

An MJO Simulated by the NICAM at 14- and 7-km Resolutions

PING LIU,* MASAKI SATOH,⁺ BIN WANG,* HIRONORI FUDEYASU,* TOMOE NASUNO,⁺
TIM LI,* HIROAKI MIURA,^{+,#} HIROSHI TANIGUCHI,⁺ HIROHIKO MASUNAGA,[@]
XIOUHUA FU,* AND H. ANNAMALAI*

* *International Pacific Research Center, SOEST, University of Hawaii at Manoa, Honolulu, Hawaii*

⁺ *Frontier Research Center for Global Change, Japan Agency for Marine-Earth Science and Technology, Kanagawa, Japan*

[#] *Department of Atmospheric Science, Colorado State University, Fort Collins, Colorado*

[@] *Hydrospheric Atmospheric Research Center, Nagoya University, Nagoya, Japan*

(Manuscript received 4 February 2009, in final form 28 March 2009)

ABSTRACT

This study discloses detailed Madden–Julian oscillation (MJO) characteristics in the two 30-day integrations of the global cloud-system-resolving Nonhydrostatic Icosahedral Atmospheric Model (NICAM) using the all-season real-time multivariate MJO index of Wheeler and Hendon. The model anomaly is derived by excluding the observed climatology because the simulation is sufficiently realistic. Results show that the MJO has a realistic evolution in amplitude pattern, geographical locations, eastward propagation, and baroclinic- and westward-tilted structures. In the central Indian Ocean, convection develops with the low-level easterly wind anomaly then matures where the low-level easterly and westerly anomalies meet. Anomalous moisture tilts slightly with height. In contrast, over the western Pacific, the convection grows with a low-level westerly anomaly. Moisture fluctuations, leading convection in eastward propagation, tilt clearly westward with height. The frictional moisture convergence mechanism operates to maintain the MJO. Such success can be attributed to the explicit representation of the interactions between convection and large-scale circulations. The simulated event, however, grows faster in phases 2 and 3, and peaks with 30% higher amplitude than that observed, although the 7-km version shows slight improvement. The fast-growth phases are induced by the fast-growing low-level convergence in the Indian Ocean and the strongly biased ITCZ in the west Pacific when the model undergoes a spinup. The simulated OLR has a substantial bias in the tropics. Possible solutions to the deficiencies are discussed.

1. Introduction

The Madden–Julian oscillation (MJO; Madden and Julian 1971, 1972, 1994) dominates tropospheric variability in the tropics on time scales of 30–60 days. The oscillation influences weather and climate variability substantially in both the tropics (e.g., Yasunari 1979; Hendon and Liebmann 1990; Lawrence and Webster 2002) and extratropics (e.g., Weickmann 1983; Ferranti et al. 1990; Lau and Chang 1992; Liebmann et al. 2004). An improved prediction of a prevalent MJO event can extend the atmospheric predictability by up to 20 days (Ferranti et al. 1990; Waliser et al. 1999). Accurately simulating and predicting MJO, however, has been a

challenge to the modeling community (Zhang 2005; Lin et al. 2006).

The MJO is powered by the latent heat released from cumulus and super cloud clusters that are modulated by large-scale circulations (Nakazawa 1988; Lau et al. 1989; Chao and Lin 1994). As a response to the convective anomaly in the west, near-boundary layer convergence leads the MJO in eastward propagation and builds up convective instability fostering the deep convection (Wang 1988; Wang and Rui 1990; Wang and Li 1994; Hendon and Salby 1994; Maloney and Hartmann 1998). Moisture anomalies thus tend to tilt westward with altitude as the MJO evolves in the eastern Indian Ocean–western Pacific (e.g., Sperber 2003; Kiladis et al. 2005). Proper mean states in atmospheric winds and sea surface temperature provide a background for the convection development so that they are disclosed as a necessary condition for AGCMs (e.g., Slingo et al. 1996) and coupled GCMs (e.g., Inness and Slingo 2003) to simulate a

Corresponding author address: Dr. Ping Liu, IPRC/SOEST, Post 409J, 1680 East–West Rd., Honolulu, HI 96822.
E-mail: pliu@hawaii.edu

realistic MJO. However, the interactions between the subgrid-scale cumulus convection and grid-scale circulation in GCMs generate and maintain the MJO fundamentally (e.g., Grabowski 2003).

Because the interactions are represented roughly by parameterizations, the simulated MJO has smaller variance, a shorter period, and less-prevalent eastward propagation than that observed in early atmospheric general circulation models (AGCM; Slingo et al. 1996) and recent climate system models (Lin et al. 2006) at 100–500-km resolutions. The MJO is still less realistic in an AGCM that has a 20-km resolution (Liu et al. 2009), indicating that the resolution is not a determining factor in conventional GCMs. Using an alternate scheme or partial change of a parameterization may improve the simulated MJO (e.g., Maloney and Hartmann 2001; Liu et al. 2005). However, the uncertainties and large sensitivities to the schemes make it difficult to conclude which aspect of a parameterization is universally essential to the simulated MJO. The uncertainties can be fundamentally reduced by using cloud-system-resolving models to explicitly resolve the convective process. When a two-dimensional cloud-resolving module at a 2-km resolution is embedded in an AGCM at a 300-km resolution over the MJO active areas so that the local interactions are represented explicitly, the simulated MJO is improved substantially in amplitude and eastward propagation (Khairoutdinov et al. 2005; Ziemiański et al. 2005). The improvement using the cloud-resolving modules as a superparameterization (Grabowski 2004) encourages treating the cumulus–circulation interactions explicitly in three-dimensional AGCMs for the MJO simulation.

A global cloud-system-resolving model integrated with realistic geophysical processes, the Nonhydrostatic Icosahedral Atmospheric Model (NICAM; Satoh et al. 2008), was recently developed. It successfully simulated the MJO event occurring in December 2006 and January 2007 using the 7-km resolution version (Miura et al. 2007). Snapshots of winds, a Hovmöller diagram of precipitation along the equatorial area, and cloud images resemble those observed in eastward propagation. The event demonstrates a clear multiscale structure compared to observed radar images (Masunaga et al. 2008). In the simulation, convectively coupled tropical waves are mixed with an MJO-like envelope propagating eastward (Nasuno et al. 2009). The two tropical cyclones with this MJO event are simulated realistically as well (Fudeyasu et al. 2008). However, the MJO in these studies is demonstrated with the climatic background and variations on shorter time scales. Whether the evolution of MJO three-dimensional structure agrees with that observed is not disclosed in detail. Nor is how the convection interacts with large-scale circulations so that the simulated MJO is

realistic, which can shed light on improving conventional GCMs. Because the model started with the output from the operational analysis system of the National Centers for Environmental Prediction (NCEP) at a 100-km resolution, how the interpolated initial condition affects the simulated MJO can be of interest. By contrasting the MJO in the previous 7- and recent 14-km runs, the sensitivity of simulated MJO to resolution in a global cloud-system-resolving model will be intriguing as well.

This study addresses these issues using the all-season real-time multivariate MJO (RMM) index of Wheeler and Hendon (2004, hereinafter WH04). The RMM framework can disclose the MJO features using daily data without any time filtering, which is appropriate for the present short-term integrations. Results show that the simulated moisture, wind, and convection anomalies associated with the MJO event have a realistic evolution in three-dimensional structures. The frictional moisture convergence mechanism (e.g., Wang 1988; Maloney and Hartmann 1998; Sperber 2003) operates to maintain the eastward propagation. Section 2 introduces the model, data, and methodology. Section 3 presents results. Section 4 includes the discussion and conclusions.

2. Model, data, and methodology

The NICAM is a global nonhydrostatic model designed for 1-km-order fine-mesh simulations. It uses an icosahedral grid system suitable for parallel computation (Tomita and Satoh 2004). The grid size is reduced gradually using a recursion method starting from level 0 with 20 triangles on the sphere (Satoh et al. 2008, their Fig. 2). Each triangle is divided into four small triangles at every recursion level. At level 9 of the recursion, the structure produces a horizontal resolution at about 14 km; and at level 10 the resolution is about 7 km. The grid structure is then smoothed by the spring dynamics. Both the 14- and 7-km resolutions use a step size of 30 s to satisfy the Courant–Friedrichs–Lewy condition. Because of the same step size and physics configurations, the sensitivity in the two simulations can be attributed to the change of horizontal resolutions. The moist processes are represented explicitly. For example, cloud physics are calculated prognostically by a simplified bulk cloud microphysical scheme (Grabowski 1998). Subgrid-scale turbulence is represented by the Nakanishi and Niino (2006) scheme that is an improved version of Mellor and Yamada (1974). Surface fluxes of heat and momentum are modeled using Louis's (1979) bulk formula. The radiation scheme is a revised version of Nakajima et al. (2000). Details of the model are referred to Satoh et al. (2008).

Using the observed weekly SST as external forcing and the NCEP operational analysis product in pressure-sigma

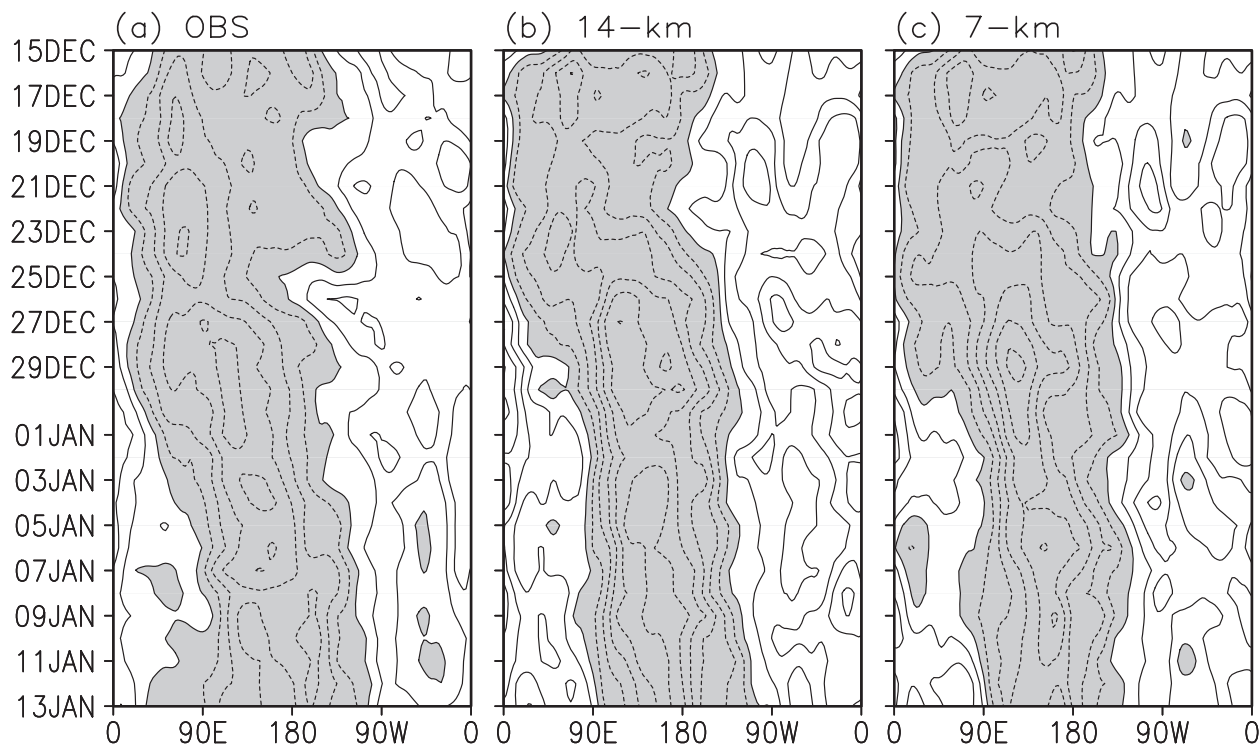


FIG. 1. The 200-hPa velocity potential ($0.5 \times 10^7 \text{ m}^2 \text{ s}^{-2}$) along the equator averaged in 15°S – 15°N during the MJO event for (a) the NCEP–NCAR reanalysis, (b) the 14-km NICAM, and (c) the 7-km NICAM. Values less than and equal to 0 are shaded.

hybrid coordinate at $1^\circ \times 1^\circ$ resolution as initial conditions, runs at 7- and 14-km resolutions were carried out for the MJO event from 15 December 2006 to 13 January 2007. The outputs are interpolated horizontally from 7 and 14 km to $2.5^\circ \times 2.5^\circ$ (about $275 \text{ km} \times 275 \text{ km}$) using a box-mean method and vertically from altitude to pressure levels at 1000, 925, 850, 700, 600, 500, 400, 300, 200, and 100 hPa using a mass-weighted algorithm. Daily mean is then derived from the spatially interpolated 6- or 1.5-hourly data for analysis.

The OLR observed by the National Oceanic and Atmospheric Administration (NOAA) satellites, the precipitation rate from the Tropical Rainfall Measuring Mission (TRMM), version 6_3B42 (Huffman et al. 2007), the surface latent heat flux, winds, and specific humidity of the NCEP–National Center for Atmospheric Research (NCAR) reanalysis (Kalnay et al. 1996) are used as observational references. All referenced variables are interpolated to daily interval, horizontal $2.5^\circ \times 2.5^\circ$ and vertical pressure levels. Daily anomalies of the model variables are derived by excluding the climatology of observations or the reanalysis from 1979 to 2007 (1998–2008 for the TRMM precipitation) because the two runs are too short in time to provide their own, because the observed climatology carries nearly null information of MJO, and—more importantly—because the simulated

30-day averages of precipitation and winds are very close to the references in the tropics, as shown in section 3 (Fig. 1). We define these fields as “simple anomalies” to differentiate them from other two types of anomalies to be described. The simulated specific humidity, however, is systematically different from that in the reanalysis in the entire tropics so that the zonal means for all variables at each pressure level are excluded from the simple anomalies for the composites (section 3b). We refer to these fields as anomalies; they are equivalent to eddy transients.

We use the RMM index of WH04 to disclose the evolution of amplitude, phase, and vertical structure, and possible mechanism for the MJO event. The index is defined by the first pair of the principal components (PCs) from a combined empirical orthogonal function (CEOF) analysis using anomalous OLR, 850-, and 200-hPa zonal winds from 1 January 1979 to 31 December 2001. The anomalous fields are derived by excluding the daily climatology, the first three harmonics of the seasonal cycle, and the interannual variability associated with ENSO. They are normalized with their global standard deviation so that each field contributes to the CEOF comparably. The first two CEOFs represent the MJO salient structure (e.g., the baroclinity and coupling between convection and circulation; Fig. 1 in WH04).

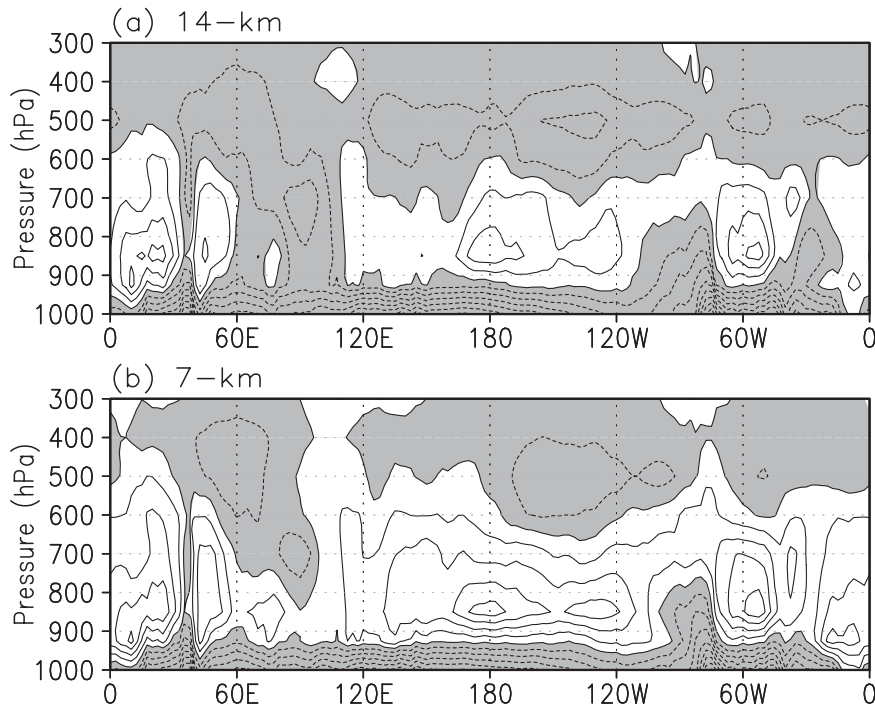


FIG. 2. Difference of the 30-day mean specific humidity from the reanalysis along the equator (averaged in 15°S – 15°N) for (a) the 14- and (b) 7-km NICAM. Values less than and equal to 0 are shaded. The contour interval is 1 g kg^{-1} .

The detailed method is referred to as WH04. The RMM can demonstrate the MJO amplitude and geographical evolution in the model compared with observations. We will use the CEOFs and variances of each variable provided by WH04 to derive the index described below.

The standardized simple anomalies from the NICAM and observations are projected onto the two CEOFs to calculate the corresponding RMMs, which differentiate slightly from those derived using the anomalous fields of WH04 (section 3). MJO phases 2–6, which are defined in the RMM diagram (WH04), are composited based on the dates for each phase. The average of several days in each phase can eliminate synoptic perturbations effectively so that the spatial filtering is not used (e.g., Hendon and Salby 1994). Inspection of the Hovmöller diagram for the convective centers to pass specific longitudes along a narrow equatorial band [e.g., 60° , 90° , 120° , and 150°E as used by Rui and Wang (1990)]; dates can be observed for composite as well. The derived days agree with those observed from the RMM diagram so that the composite structures are similar. It is noteworthy that model OLR is used for deriving the RMMs but not for composites because it has a reasonable pattern but much larger value in the tropics (see Fig. 12 in the discussion). The precipitation represents convection well as a direct product and it is used in the composites.

3. Results

a. The MJO event

The simulated MJO event resembles that observed, as illustrated roughly by a Hovmöller diagram of precipitation in time–longitude space (Fig. 4b in Miura et al. 2007). Here we show the evolution of 200-hPa velocity potential in the equatorial area averaged between 15°S and 15°N during the 30-day integrations (Fig. 1). The velocity potential in the reanalysis (Fig. 1a) is about $-1 \times 10^7 \text{ m}^2 \text{ s}^{-2}$ near 60°E around 15 December 2006. It is strengthened to $-2.5 \times 10^7 \text{ m}^2 \text{ s}^{-2}$ near 70°E on 23 December. This center moves to the date line around 13 January 2007. An eastward propagation is discernible, for example, from the negative values (shaded). The strengthening center and eastward-propagation patterns are simulated well by the 14- and 7-km NICAM except that the central values are slightly higher than those in the reanalysis (Figs. 1b,c). The simulated winds have a similar pattern and values to the reanalysis in the tropical troposphere (not shown; Fig. 2 in Miura et al. 2007). Because of such similarities, the model anomalies for winds, OLR, precipitation, and surface latent heat fluxes are derived by excluding the climatology of observations or the reanalysis. However, the simulated specific humidity has a systematic difference from the reanalysis as shown in Fig. 2. In both model versions, a

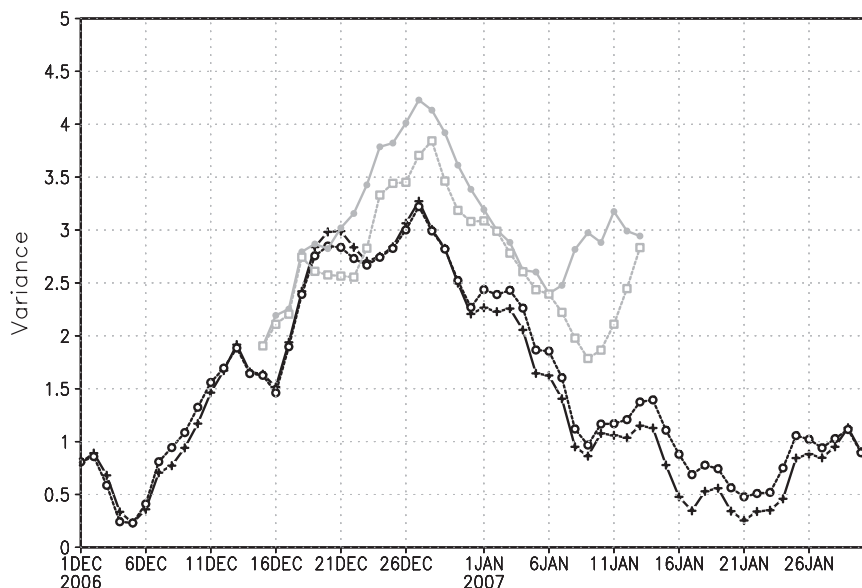


FIG. 3. Evolution of the MJO event in amplitude represented by $(\text{RMM1}^2 + \text{RMM2}^2)^{1/2}$. The black, solid, plus curve is derived using the anomalous fields described in WH04; others use simple anomalies by excluding the observed climatology for observations (black, dashed, open), the 14-km NICAM (gray, solid, closed), and the 7-km NICAM (gray, dashed, square).

much drier boundary layer between the surface and 900 hPa is produced along the equator (averaged in 15°S – 15°N). The difference is as much as -4 g kg^{-1} . In the layer between 900 and 600 hPa, it is much wetter in the NICAM, particularly in the 7-km version. The specific humidity decreases again systematically in the layers above 600 hPa. Such systematic difference is likely induced by the boundary layer scheme incorporating with the explicit microphysics. Because of the systematic difference and our focus on the MJO fluctuations, the zonal means for all variables at each pressure level are excluded from the simple anomalies for the composites in section 3b.

After the simple anomalies of OLR, 850-, and 200-hPa zonal winds are derived, they are standardized with the global standard deviation and then projected onto the first pair of COEFs provided by WH04 to derive the corresponding principal components of RMM1 and RMM2. The time series of $(\text{RMM1}^2 + \text{RMM2}^2)^{1/2}$ can disclose the MJO evolution in amplitude. WH04 provides a 91-day running mean of the series. In an extended version (not shown), the current MJO has an amplitude only about 1/3 of other 10 strong events occurring in the past 20 years. Moreover, the 91-day filtering is not suitable for the 30-day simulations. Figure 3 shows the unfiltered series of RMM amplitude for the observations using anomalous fields and for both observations and the NICAM using simple anomalies. The two curves for observations (black) coincide with each other from 1 to 31 December 2006 and have a slight

difference thereafter, indicating that the simple anomalies (black-dashed-open curve in Fig. 3) can disclose the MJO event fairly well. The MJO event becomes detectable with an amplitude larger than 1 near 8 December 2006, which agrees well with the Hovmöller diagram of precipitation (Fig. 4b in Miura et al. 2007). The event peaks with an RMM amplitude of 3.3 near 27 December, then decays back to less than 1 near 16 January 2007. The detectable cycle lasts about 40 days.

The RMM amplitude evolution in the two NICAM versions generally agrees well with that observed (gray curves in Fig. 3). The simulated event starts on 15 December 2006 with slightly higher amplitude. This small difference can originate from the spinup of interpolated initial conditions from the NCEP operational analysis in a vertical sigma-pressure coordinate and at horizontal $1^{\circ} \times 1^{\circ}$ resolution. The difference remains small until 21 December 2006 in the 14-km version and until 23 December in the 7-km version, indicating an improvement due to the higher resolution. The simulated event by 14-km NICAM peaks at the same day as that observed, but the RMM amplitude reaches nearly 4.2, about 30% larger than that observed. One day later, the MJO in the 7-km version peaks with the RMM amplitude of 3.8, which is improved but still high. The MJO then decays with a higher amplitude. A small turnaround occurs near the RMM amplitude of 1 on 9 January 2007 in observations and rebounds to near 1.4 on 15 January. However, the turnaround occurs on 6 January in the 14-km

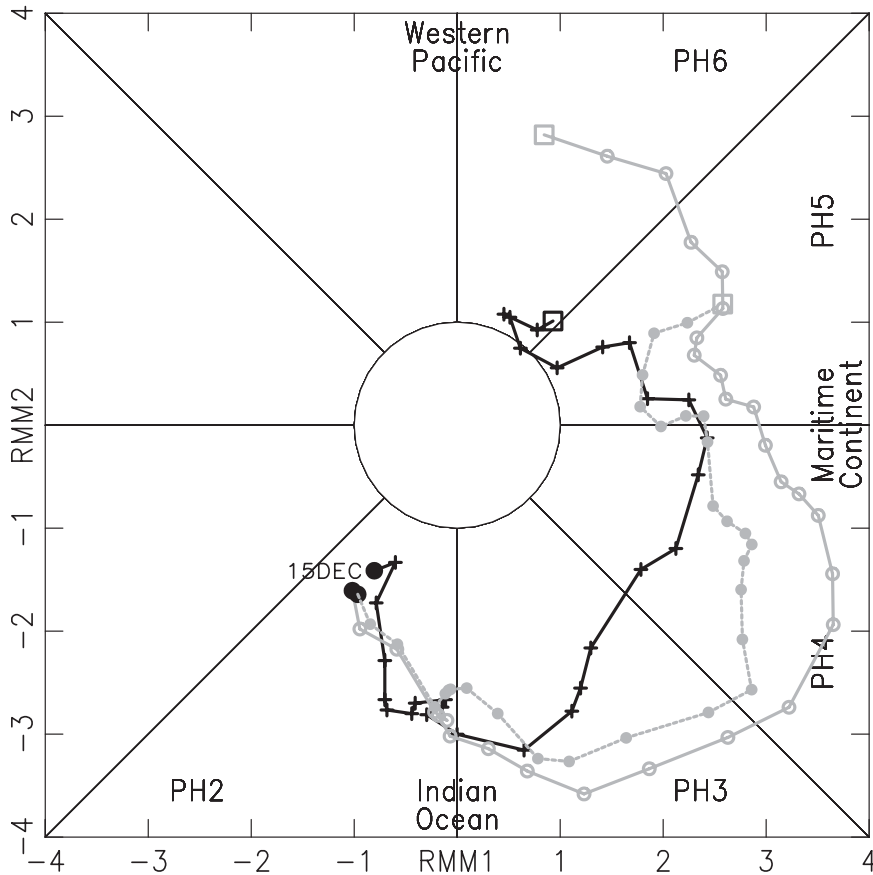


FIG. 4. RMM diagram for the MJO event in observations (black, solid, plus), the 14-km NICAM (gray, solid, open), and the 7-km NICAM (gray, dashed, closed).

version and regains the amplitude up to 3.2 on 11 January. The 7-km version improves the simulation by a turnaround occurring on the same day as that observed, but the amplitude is still much higher and reaches nearly 3 on 13 January, indicating that the simulated event might last longer if the integration continues. Similar agreement occurs in the geographical evolution of the MJO event as shown in the RMM diagram.

Eight phases of an MJO event are defined in the RMM diagram (WH04) with each in the 1/8 portion as shown in Fig. 4. Phases 2 (marked as PH2) and 3 (PH3) correspond to an enhanced convection in the Indian Ocean while 4 (PH4) and 5 (PH5) in the Maritime Continent and 6 (PH6) in the central-west Pacific. The truncated event in observations (black) starts from 15 December over the western Indian Ocean then evolves through phase 6 in the western Pacific. The simulated event (gray curves) agrees well with that observed in phase 2, early phase 3, and early phase 5. It has a similar evolution but higher RMM values in remaining phase 3, most of phase 4, and phase 6. A close inspection of the diagram indicates that the simulated event grows faster than that

observed in phases 2 and 3. Dates for other phases are different as well, which is summarized in Table 1.

The striking difference in Table 1 occurs in phases 2 and 3. Phase 2 ends on 26 December 2006 in observations, while on 21 December in the two model versions, indicating that a faster growth rate is simulated in the Indian Ocean. This fast growth is caused by the low-level convergence, which will be shown in the composite structures below. During the 12 days of phase 2, two westward-moving synoptic waves west of 90°E can be observed in the Hovmöller diagram of precipitation (e.g., Fig. 4b of Miura et al. 2007). Both waves are simulated fairly well in the two NICAM versions (not

TABLE 1. Dates for each phase from the RMM diagram.

| | Obs | 14 km | 7 km |
|---------|--------------|--------------|--------------|
| Phase 2 | 15–26 Dec | 15–21 Dec | 15–21 Dec |
| Phase 3 | 27–30 Dec | 22–26 Dec | 22–27 Dec |
| Phase 4 | 31 Dec–3 Jan | 27 Dec–2 Jan | 28 Dec–5 Jan |
| Phase 5 | 4–8 Jan | 3–10 Jan | 6–13 Jan |
| Phase 6 | 9–13 Jan | 11–13 Jan | — |

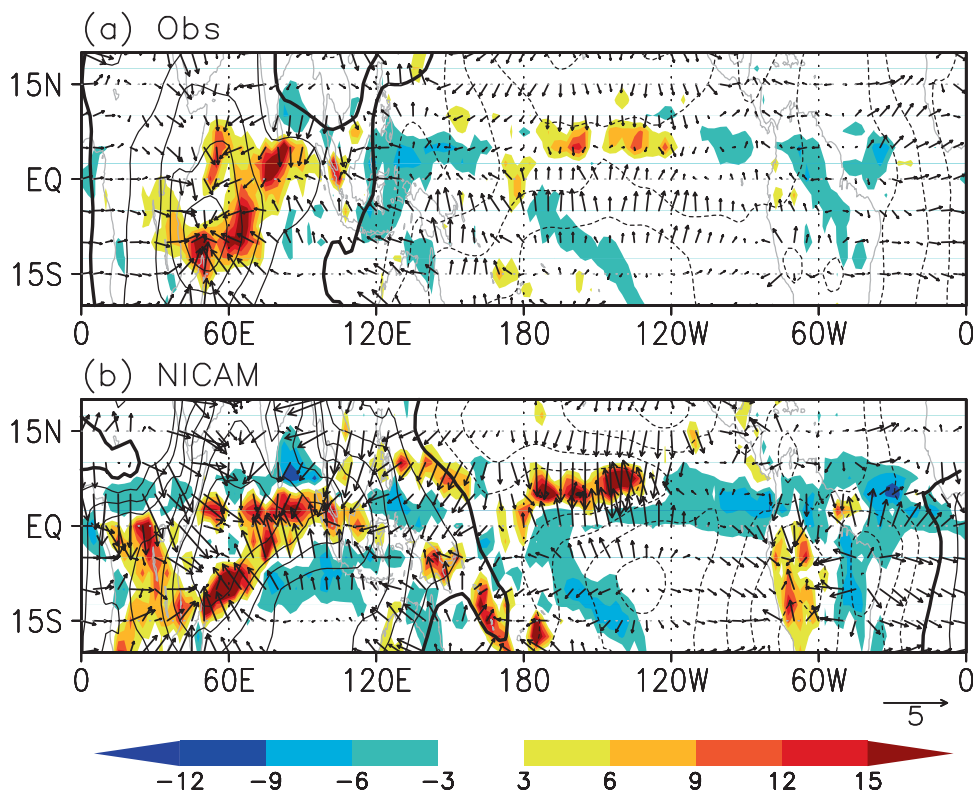


FIG. 5. Composites anomalies for phase 2 of the MJO event in (a) observations and (b) the 7-km NICAM. Contours represent the velocity potential (interval is $1 \times 10^7 \text{ m}^2 \text{ s}^{-2}$ with thick, black as 0) at 925 hPa and vectors (m s^{-1}) for the divergence wind at this level. The shading represents the precipitation rate (mm day^{-1}) from the (a) TRMM and (b) NICAM.

shown) except the model convection crosses 90°E earlier. As indicated in the RMM diagram, the simulated event thus starts earlier and ends earlier in phase 3; but lasts longer in phases 4 and 5. The 14-km version simulates comparable dates for phase 6 but the 7 km ends the event in phase 5. This early ending corresponds to a much higher amplitude of RMM in Fig. 1. By assuming the event has a similar structure during the days in each phase, composites of consecutive phases will provide the evolution in vertical structures. Because the composites difference is small in the two runs, only the 7-km case is compared with observations below.

b. Phase composites

Previous studies (e.g., Hendon and Salby 1994; Maloney and Hartmann 1998; Sperber 2003; WH04; a review by Zhang 2005) have disclosed similarly salient structures of an MJO during successive development stages in spite of different methods used. In the western-central Indian Ocean corresponding to phase 2 in the RMM framework, convection is initiated over low-level easterly anomalies and then matures over the intersection of low-level easterly and westerly anomalies. Moisture

anomalies generally are in phase with the convection without an apparently westward tilt with height. The structures are different in the Maritime Continent and the western Pacific. Boundary layer convergence forced by the convection in the west builds up moist instability, fostering deep convection during which low-level westerly anomalies dominate. The moisture anomalies thus have a clearly westward tilt structure with height. These distinct structures of MJO are summarized as the models I and II in a schematic diagram by Zhang (2005, their Fig. 6). The following composites for phases 2–6 of the MJO will demonstrate that these structures occur in this event as well and they are maintained by the frictional moisture convergence mechanism.

Phase 2 is the average of 12 days in observations and of 7 days in the NICAM (cf. Table 1). During this phase, convection is enhanced near ($13^\circ\text{--}1^\circ\text{S}$, $60^\circ\text{--}70^\circ\text{E}$) and ($0^\circ\text{--}3^\circ\text{N}$, $85^\circ\text{--}90^\circ\text{E}$) with a precipitation anomaly of over 15 mm day^{-1} (Fig. 5a). It is weaker to the west of 60°E , corresponding well to the westward-propagating waves as observed in the Hovmöller diagram (not shown). Shallow convection is discernible up to 110°E near the equator. Suppressed convection occurs in the Maritime

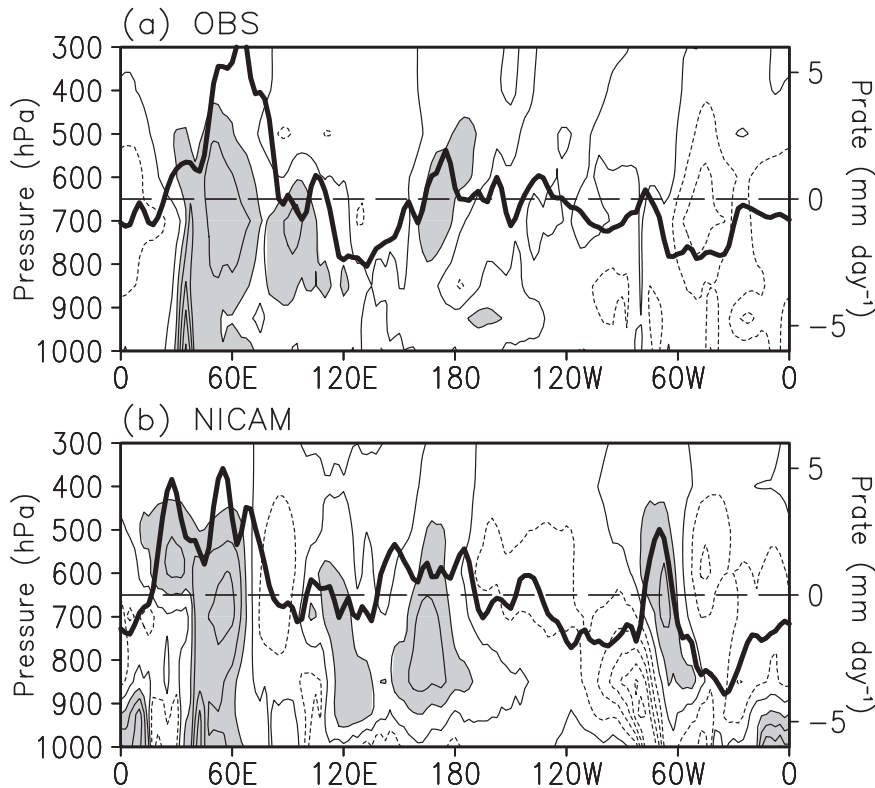


FIG. 6. As in Fig. 5, but the contours represent the specific humidity (interval 0.5 g kg^{-1}) with shaded values greater than 0. The thick, black curve is for the precipitation rate (mm day^{-1}) in (a) TRMM and (b) NICAM. All values are along the equator (averaged between 15°S and 15°N).

Continent–west Pacific, forming a dipole structure at zonal wavenumber 1 with the enhanced convection in the Indian Ocean (Fig. 5a). The convergence at 925 hPa, shown by the positive anomalies of velocity potential (contours) and convergent wind vectors, occurs in the whole Indian Ocean fostering the convection. It approaches the Maritime Continent, indicating a lead in eastward propagation. Weak divergence occurs in the east Pacific and weak convergence in the rest of the Western Hemisphere; the velocity potential has a zonal wavenumber 1 structure as well. The convection and low-level convergence develop a typical structure for an MJO developing phase in the Indian Ocean (e.g., Hendon and Salby 1994; Sperber 2003). The simulated convection generally agrees with that observed in the Indian Ocean (Fig. 5b) except for relatively larger values in the eastern Indian Ocean and southern Africa. Correspondingly, the simulated convergence extends to 160°E near the equator (Fig. 5b); and the center is near 60°E about twice stronger than that observed. Both convection and convergence are about 20° – 30° farther eastward than those observed, showing a faster growth rate. It is noteworthy that the ITCZ in the central Pacific north of the equator is much

stronger than that observed, which can be caused by the apparently stronger low-level convergence. This fast growth of low-level convergence is probably due to the spinup of upscaled initial conditions from resources at a coarse resolution (see the discussion).

Figure 6 shows the vertical structure of specific humidity (contours with shading) with precipitation (thick black curve) anomalies averaged over 15°S – 15°N during phase 2 along the equator. Corresponding to the low-level convergence, the positive moisture anomalies (shaded) near 60°E are in concert with the developing convection (thick black curve) in both observations and the NICAM. They expand from the surface up to 450 hPa. Meanwhile, the humidity shows a developing west-tilt structure along the equatorial Eastern Hemisphere. Small positive anomalies occur to the east of the convection in lower levels to the surface.

Model I of MJO in Zhang (2005) and the schematic diagram in Sperber (2003) predict that the maturing convection near 60°E in phase 2 corresponds to the intersection of low-level westerly and easterly anomalies. This structure is clearly shown in Fig. 7. Easterly anomalies (dashed contours) occur right under the convective

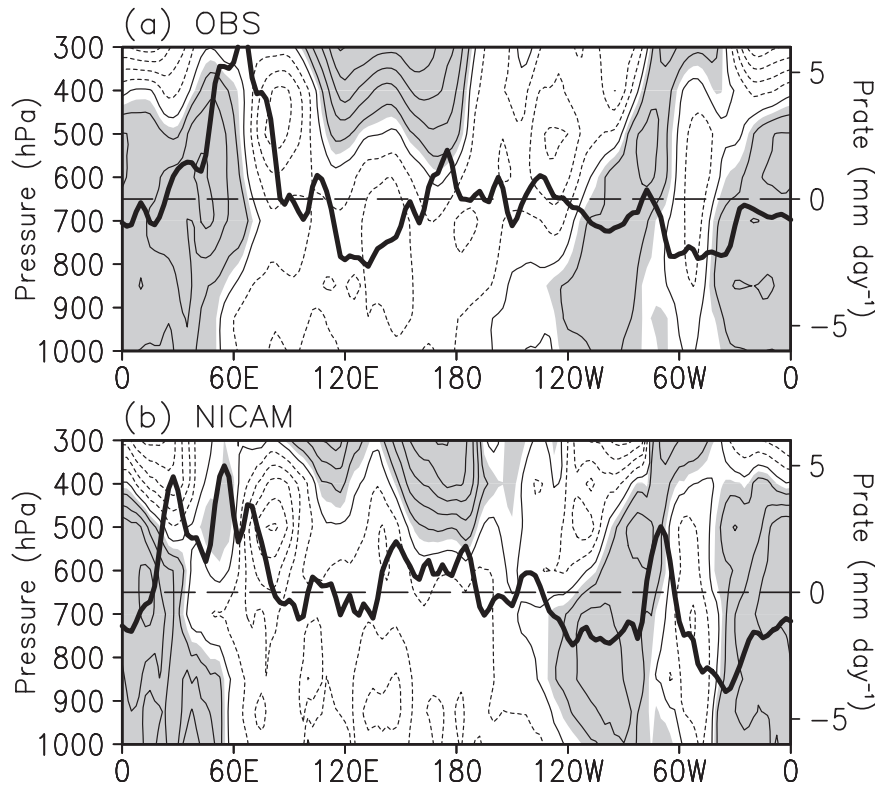


FIG. 7. As in Fig. 6, but the contours represent the zonal wind (interval 0.5 m s^{-1}).

center (thick black curve) and extend from near 60°E to 120°W in the layer of 1000–600 hPa; while westerly anomalies (solid contours with shading) dominate from 60°E west to 50°W near the surface to 400 hPa. In the layers above, the phase is nearly reversed, indicating a baroclinic structure. The easterly anomalies appear as a Kelvin wave response and the westerly anomalies appear as a Rossby wave response. The NICAM has realistically reproduced this complicated structure except that the westerly wind anomalies are weaker in the 800–500-hPa layer near $50^\circ\text{--}60^\circ\text{E}$ (Fig. 7b).

Observed convection anomalies in phase 3 (not shown) transits to negative in the central Indian Ocean near 60°E , turns to weak and shallow in the east Maritime Continent to the date line, and matures near $5^\circ\text{S}\text{--}0^\circ$, $90^\circ\text{--}100^\circ\text{E}$. Corresponding to this transition, the 925-hPa convergence (not shown) weakens in the central Indian Ocean, shifts its center to the west Maritime Continent, and edges near the date line, fostering convection in the east Maritime Continent and West Pacific. The velocity potential and convergent wind are still stronger than that observed. The simulated convection by two NICAM versions has a similar pattern to that observed (not shown) except for its persistence in the west Indian Ocean, and that it damps in the east Indian Ocean. The ITCZ is still strong and extends westward to connect the

convection in the east Maritime Continent, producing a faster growth than that observed. The persistently strong ITCZ indicates a bias in the mean state of the model.

The specific humidity anomalies along the equatorial area have a vertical structure matching the surface convergence and convection anomalies in observations during phase 3 (not shown). It becomes negative from the surface to 500 hPa near 60°E . The positive anomalies have a center at 700 hPa near 120°E and extend eastward at lower levels, indicating that the frictional moisture convergence is functioning. Very similar structures are simulated by the two NICAM versions (not shown) except that the anomalies are somewhat weaker over the Maritime Continent–west Pacific.

As a wave response to the convective heating centered near 120°E along the equator, observed zonal winds (not shown) become westerly anomalies from 850 to 500 hPa and easterly aloft from equatorial Africa to 120°E while easterly from the surface to 400 hPa and westerly aloft in the rest of the equatorial areas. The baroclinic structure of zonal winds has a zonal wavenumber 1 feature. This structure is simulated well by the two NICAM versions (not shown).

During phase 4, observed convection anomalies (shadings in Fig. 8a) return back to near normal in the west Indian Ocean, and become more suppressed near 90°E

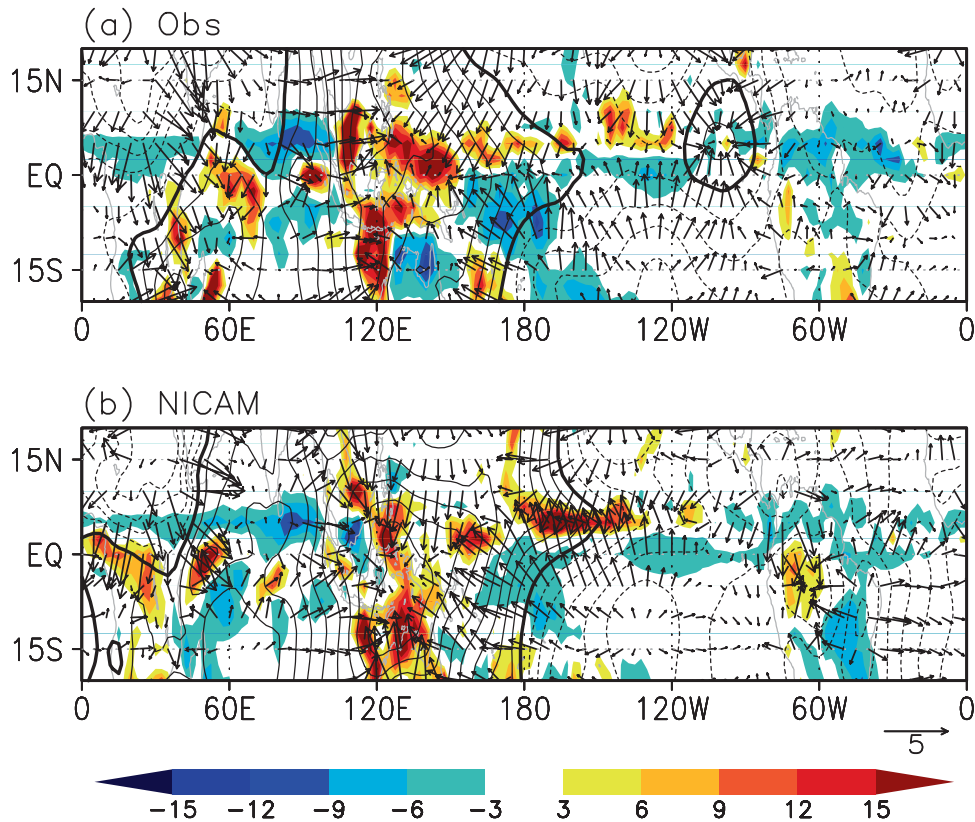


FIG. 8. As in Fig. 5, but for phase 4.

north of the equator with a central precipitation anomaly of -12 mm day^{-1} . Enhanced convection prevails over the Maritime Continent and west Pacific with precipitation anomalies of over 15 mm day^{-1} in $115^{\circ}\text{--}150^{\circ}\text{E}$. The other equatorial areas have weak convective anomalies. The observed convergence at 925 hPa (contours and vectors in Fig. 8a) is weakened in Africa–Indian Ocean, while strengthened in the Maritime Continent–west Pacific with its center shifts to $120^{\circ}\text{--}150^{\circ}\text{E}$ near the equator. The convergence at this level crosses the date line. The simulated convection anomalies (shadings in Fig. 8b) have a similar pattern to that observed: suppressed convection in the Indian Ocean and enhanced precipitation in the Maritime Continent and west Pacific. The convection over ITCZ in the central and eastern Pacific is still much stronger than that observed, which indicates the bias of mean state. The simulated convergence at 925 hPa (contours and vectors in Fig. 8b) has a center near $120^{\circ}\text{--}150^{\circ}\text{E}$ around the equator, very close to that observed. However, positive velocity potential and convergent vectors are generally stronger in this area and much stronger over the ITCZ than the observations. The stronger low-level winds contribute to the much higher amplitude of RMM near this phase (Fig. 3).

The vertical structures in phase 4 repeat those illustrated by Sperber (2003) and Zhang (2005). Observed anomalies of specific humidity (contours in Fig. 9a) become weakly positive from the surface to 500 hPa in $40^{\circ}\text{--}70^{\circ}\text{E}$ averaged between 15°S and 15°N , and strongly negative from the surface to 500 hPa in $70^{\circ}\text{--}100^{\circ}\text{E}$. The moisture anomalies correspond to the suppressed convection as shown by the averaged TRMM precipitation (thick black curve) and shadings in Fig. 8a. In relation to the strong convection anomalies in the Maritime Continent–west Pacific (thick black curve in Fig. 9a and shadings in Fig. 8a), strong positive anomalies of moisture extend from the surface to 400 hPa near 120°E and to 600 hPa near 160°E , demonstrating an apparent westward tilt with height. Weak positive anomalies are building up in the boundary layer from near $170^{\circ}\text{E}\text{--}150^{\circ}\text{W}$, indicating that the frictional moisture convergence mechanism is functioning. The simulated vertical structure has a very similar pattern and a close relation between moisture and convection anomalies (Fig. 9b) compared to that observed. Weak/negative moisture anomalies correspond to a suppressed convection in the Indian Ocean; while the reversed anomalies prevail over the Maritime Continent–west Pacific. Moisture anomalies in the boundary layer

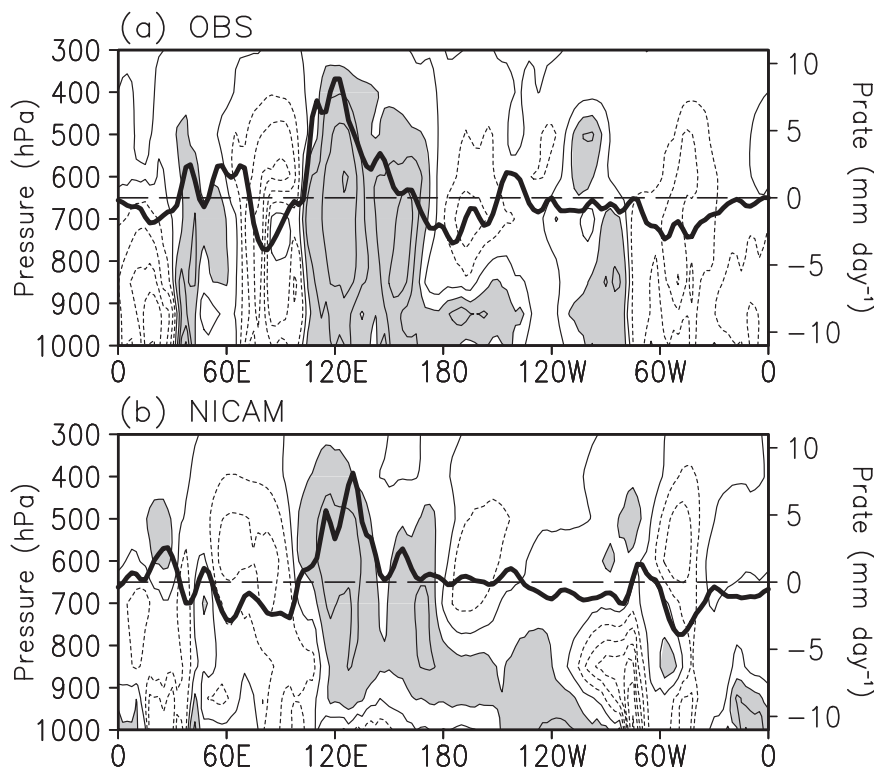


FIG. 9. As in Fig. 6, but for phase 4.

are clearly built up, indicating that the frictional moisture convergence mechanism operates (cf. Fig. 8b). It is noteworthy that the specific humidity has relatively smaller anomalies in the NICAM than that in the reanalysis. This is likely due to the systematic difference as shown in Fig. 1.

Zonal wind anomalies in phase 4 have the typical vertical structure disclosed in Sperber (2003) and summarized in Zhang (2005) as well. In observations (contours and shadings in Fig. 10a), westerly anomalies prevail from the surface to nearly 400 hPa in the Eastern Hemisphere up to 130°E except that easterly anomalies occur below 850 hPa and above 600 hPa in 60°–90°E. The convection anomaly maximum (thick black curve in Fig. 10a) occurs near 120°E, very close to the westerly anomaly maxima from the surface to 500 hPa. At the same time, easterly anomalies dominate from the surface to near 400 hPa in the rest of the equatorial Pacific with a center at 700 hPa around the date line. Convection is weakening with strengthening easterly anomalies. The patterns are reproduced realistically in the NICAM. Westerly anomalies occur in the deep layer to the west of the enhanced convection and easterly anomalies occur to the east. However, the low-level zonal wind anomalies in the NICAM (Fig. 10b) are weaker partly because of the excluded zonal means. The simulated

wind anomalies in the upper levels extend farther downward so that the baroclinic structure is more pronounced than in observations in particular from 150°E to 130°W. Such small differences do not negate that the salient vertical structures of the MJO are reproduced realistically by the NICAM. Phases 5 and 6 are the damping stage for the current event. The structures in observations (not shown) are generally similar to those of phase 4 with centers shifting more eastward. The simulated structure resembles that observed as well (not shown). The 14-km NICAM performed generally the same as the 7-km version although small differences are produced.

4. Conclusions and discussion

The MJO event occurring from December 2006 to January 2007 is simulated realistically in amplitude evolution, eastward propagation, and three-dimensional structures by the NICAM at 14- and 7-km resolutions as disclosed using the index of WH04. The frictional moisture convergence mechanism operates to maintain the simulated MJO event so that the vertical structures of moisture and wind anomalies are realistic. Such success can be attributed to the explicit representation of the interactions between cumulus clouds and large-scale circulations. The

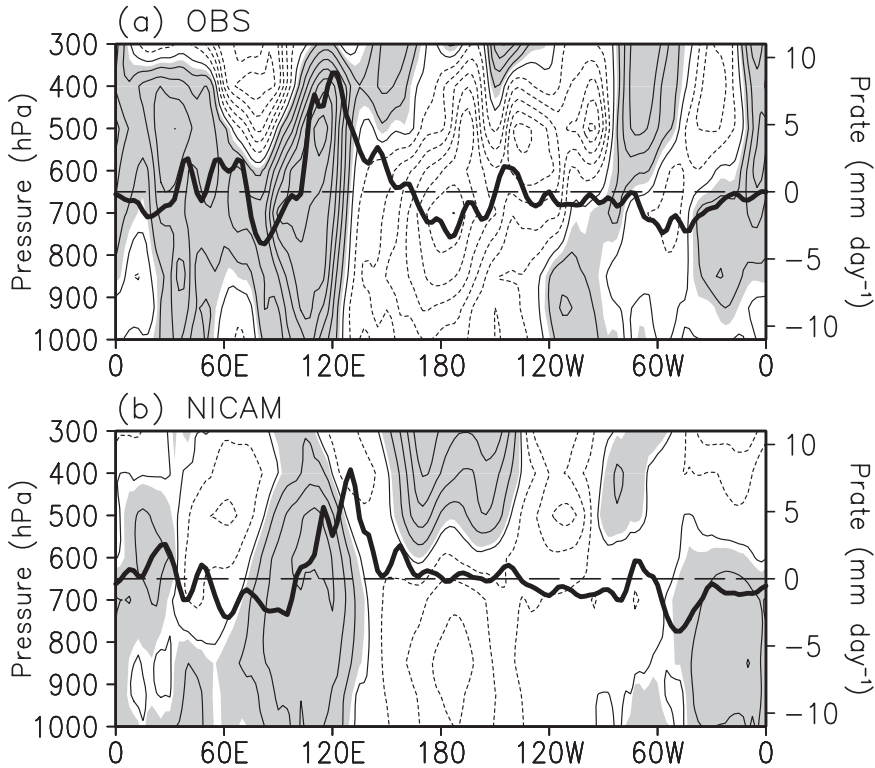


FIG. 10. As in Fig. 7, but for phase 4.

promising simulation of this MJO event and perturbations on smaller scales with the NICAM suggests that explicitly resolved microphysics can take the place of parameterizations for the future dynamical subseasonal range fore-

cast. Successive studies will disclose the interactions on very short time scales to specifically guide improving the parameterization schemes for climate models. In spite of the overall success, small deficiencies occur in higher peak amplitudes and faster-evolving phases 2 and 3 than observations, which are improved slightly in the 7-km simulation. Other possible mechanism for the MJO and causes to the fast growth of phases 2 and 3 are discussed below, followed by possible corrections.

In the central Indian Ocean, because the climatology of low-level wind can be easterly and convection development can occur over easterly anomalies (phase 2 in Fig. 7), the wind-induced surface heat exchange (WISHE; Neelin et al. 1987; Emanuel 1987) mechanism may operate for

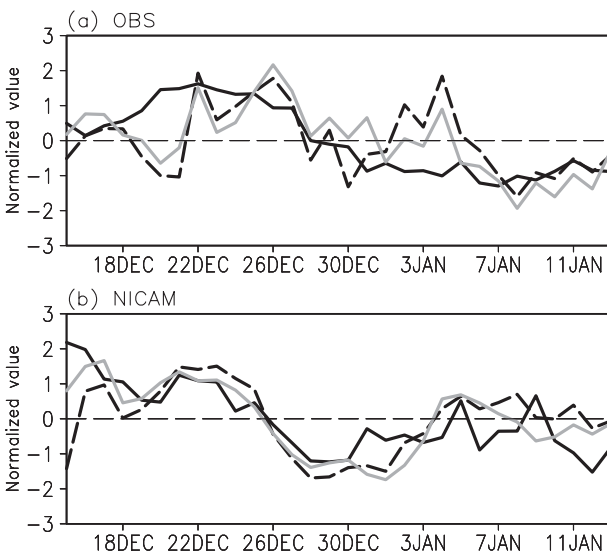


FIG. 11. Evolution of anomalies for precipitation rate (black solid), surface latent heat flux (black dashed), and wind speed at 10 m (gray) over central Indian Ocean (10°S–10°N, 70°–90°E mean) during the MJO event for (a) observations and the reanalysis and (b) the 7-km NICAM. Values are standardized for comparison.

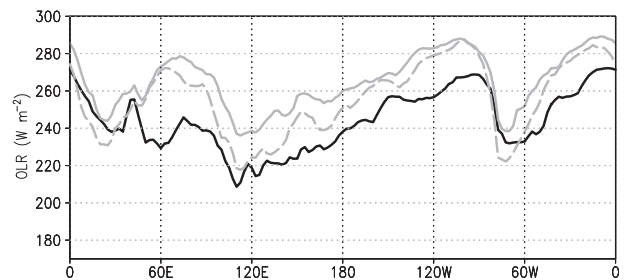


FIG. 12. The 30-day mean of OLR ($W m^{-2}$) along the equator (10°S–10°N mean) from NOAA satellite observations (black), the 14-km (gray solid), and 7-km (gray dashed) NICAM.

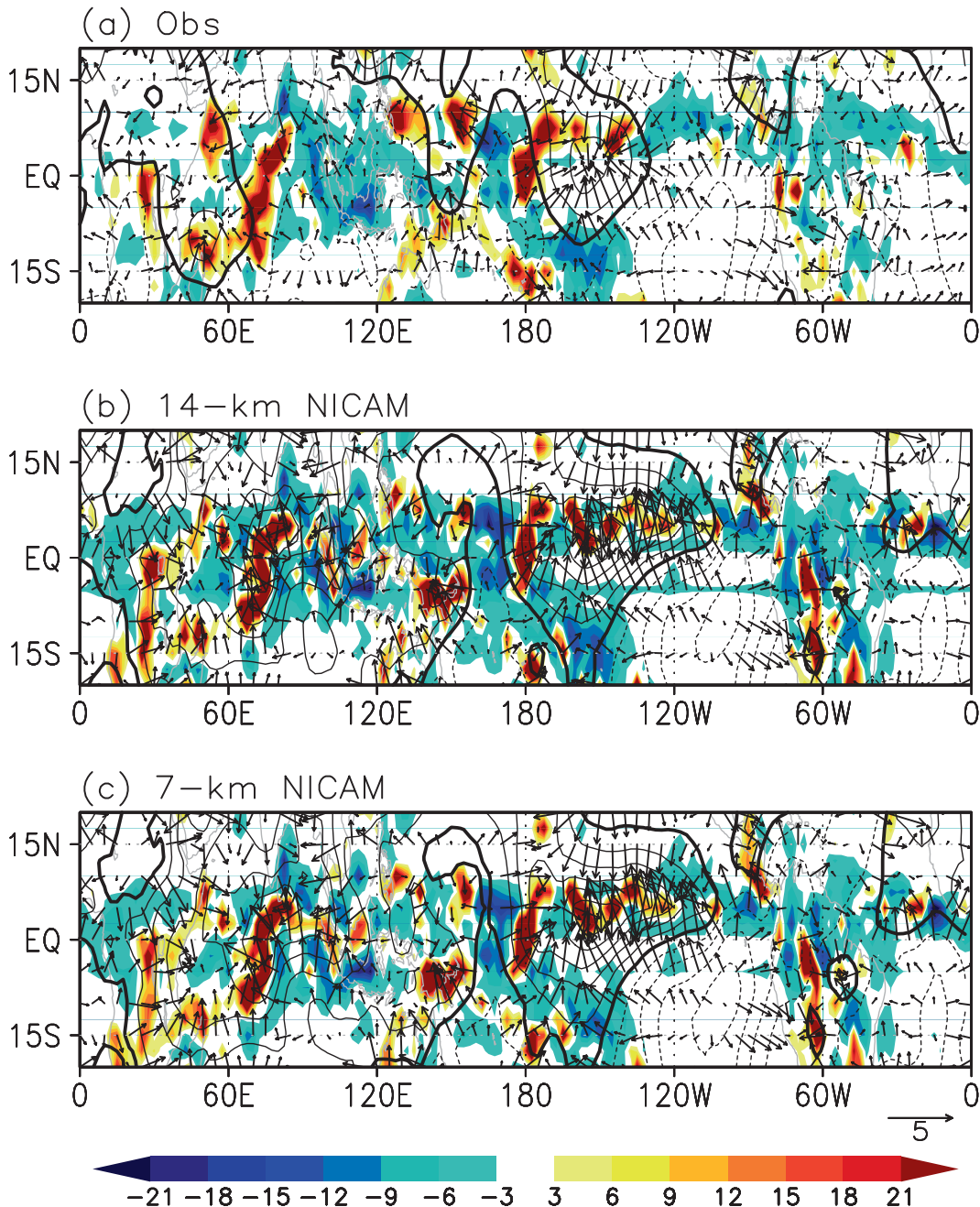


FIG. 13. The first day mean anomalies for velocity potential (contours; interval is $1 \times 10^6 \text{ m}^2 \text{ s}^{-2}$ and thick black is 0), divergent wind vector (m s^{-1}) at 925 hPa. Shaded are precipitation rate (mm day^{-1}) for (a) TRMM, (b) 14-km NICAM, and (c) 7-km NICAM.

the local MJO development, which was shown in GCM studies (e.g., Maloney and Sobel 2004; Liu et al. 2005). Nevertheless, WISHE does not have a favorable condition in this MJO event as shown in Fig. 11. The curve of surface latent heat flux (black and dashed) follows closely that of the wind speed at 10 m (gray) in both the reanalysis and NICAM. There is no clear lead in time of the negative

anomalies for surface latent heat flux and positive sea surface temperature (not shown) to the enhanced convection (black and solid). Instead, the enhanced convection leads the negative flux during 17–22 December in the reanalysis; and it is in phase with the positive flux during the first several days in the model. This is not a favorable structure for WISHE, which requires that negative surface

latent heat flux leads convection in the east by 1–2 pentads (e.g., Maloney and Sobel 2004).

It is noteworthy that the enhanced convection, represented by positive precipitation anomalies (black solid curve in Figs. 11b), persists up to 25 December 2006, longer than the OLR anomalies shown in the RMM diagram (Fig. 4). This is because the simulated OLR is not connected as closely with precipitation as in observations. Although Inoue et al. (2008, their Fig. 15) showed that the latitudinal bias of OLR is small in the tropics relative to observations when averaged in 90°E–160°W, the bias is prominent in the MJO active areas. Figure 12 shows the 30-day mean total OLR along the equator (10°S–10°N) in observations and the two NICAM versions. The simulated OLR has a similar pattern to that observed so that the standardized series are used to derive the RMM index (Figs. 3 and 4). However, a large bias occurs from 50° to 90°E and from 70°W to the Greenwich meridian in both model versions. The 7-km version improves the simulation but the bias is still large; thus, the OLR was not used for composites for the MJO structures. The large bias is likely induced by the separation of the explicit moist process and the radiation transfer scheme. The boundary layer process can contribute to the bias as well considering the systematic difference of the simulated moisture compared with that in the reanalysis (Fig. 2). A comprehensive microphysics package and an improved boundary layer scheme will be incorporated with the next version of NICAM so as to reduce the bias.

The strikingly fast growth of phases 2 and 3 can originate from the low-level convergence and biased ITCZ in the initialization. Figure 13 shows the first-day average of simulated convection, 925-hPa velocity potential, and divergent vector compared with observations. Small difference of winds in the initial condition produced by interpolation becomes large after the 1-day spinup. For example, although enhanced convection occurs in a slope area of 70°–95°E and 13°S–5°N in both observation and two NICAM versions (shaded in red), the simulated convection has already extended to the Maritime Continent. Both the velocity potential and wind vectors show that the corresponding convergence has developed to be much stronger than that observed in the Indian Ocean–Maritime Continent. More importantly, the ITCZ in the central and eastern Pacific are developing dramatically. Rotational wind vectors at lower levels (not shown) grow fast in the Indian Ocean–west Pacific as well. Such faster growth demands an effective method for the initialization, for example, a four-dimensional variational data analysis (4DVAR) or a Karman filter as widely used in the operational global systems for medium-range weather forecast. Moreover, the stronger ITCZ is persistent in all the phases 2–5 as a

bias in the two NICAM versions. The 7-km version has a slight improvement. Considering the other improvements in the 7-km version (e.g., Fig. 1), the NICAM at higher resolutions can be tested to reduce this bias besides the improved microphysical package.

Acknowledgments. This study is supported by the Japan Agency of Marine Science and Technology (JAMSTEC) and NASA Grant NNX07AG53G through their sponsorship of the International Pacific Research Center (IPRC). We thank Dr. David A. Randall and Ms. Diane Henderson for helpful comments. The CEOFs and variance for anomalous OLR, 850-, and 200-hPa zonal winds are provided by the Bureau of Meteorology Research Centre, Australia, through their Web site <http://www.bom.gov.au/bmrc/clfor/cfstaff/matw/maproom/RMM/>.

REFERENCES

- Chao, W. C., and S.-J. Lin, 1994: Tropical intraseasonal oscillation, super cloud clusters, and cumulus convection schemes. *J. Atmos. Sci.*, **51**, 1282–1297.
- Emanuel, K. A., 1987: An air-sea interaction model of intraseasonal oscillation in the Tropics. *J. Atmos. Sci.*, **44**, 2324–2340.
- Ferranti, L., T. N. Palmer, F. Molteni, and E. Klinker, 1990: Tropical-extratropical interaction associated with the 30–60 day oscillation and its impact on medium and extended range prediction. *J. Atmos. Sci.*, **47**, 2177–2199.
- Fudeyasu, H., Y. Wang, M. Satoh, T. Nasuno, H. Miura, and W. Yanase, 2008: The global cloud-system-resolving model NICAM successfully simulated the lifecycles of two real tropical cyclones. *Geophys. Res. Lett.*, **35**, L22808, doi:10.1029/2008GL036003.
- Grabowski, W. W., 1998: Toward cloud resolving modeling of large-scale tropical circulations: A simple cloud microphysics parameterization. *J. Atmos. Sci.*, **55**, 3283–3298.
- , 2003: MJO-like coherent structures: Sensitivity simulations using the cloud-resolving convection parameterization (CRCP). *J. Atmos. Sci.*, **60**, 847–864.
- , 2004: An improved framework for superparameterization. *J. Atmos. Sci.*, **61**, 1940–1952.
- Hendon, H. H., and B. Liebmann, 1990: A composite study of onset of the Australian summer monsoon. *J. Atmos. Sci.*, **47**, 2227–2240.
- , and M. L. Salby, 1994: The life cycle of the Madden–Julian oscillation. *J. Atmos. Sci.*, **51**, 2225–2237.
- Huffman, G. J., and Coauthors, 2007: The TRMM Multisatellite Precipitation Analysis (TMPA): Quasi-global, multiyear, combined-sensor precipitation estimates at fine scales. *J. Hydrometeorol.*, **8**, 38–55.
- Inness, P. M., and J. M. Slingo, 2003: Simulation of the Madden–Julian oscillation in a coupled general circulation model. Part I: Comparison with observations and an atmosphere-only GCM. *J. Climate*, **16**, 345–364.
- Inoue, T., M. Satoh, H. Mirua, and B. Mapes, 2008: Characteristics of cloud size of deep convection simulated by a global cloud resolving model over the western tropical Pacific. *J. Meteor. Soc. Japan*, **86A**, 1–15.
- Kalnay, E., and Coauthors, 1996: The NCEP/NCAR 40-Year Reanalysis Project. *Bull. Amer. Meteor. Soc.*, **77**, 437–471.

- Khairoutdinov, M., D. Randall, and C. DeMott, 2005: Simulations of the atmospheric general circulation using a cloud-resolving model as a superparameterization of physical processes. *J. Atmos. Sci.*, **62**, 2136–2154.
- Kiladis, G. N., K. H. Straub, and P. T. Haertel, 2005: Zonal and vertical structure of the Madden–Julian oscillation. *J. Atmos. Sci.*, **62**, 2790–2809.
- Lau, K.-M., and F. C. Chang, 1992: Tropical intraseasonal oscillation and its prediction by the NMC operational model. *J. Climate*, **5**, 1365–1378.
- , L. Peng, C. H. Sui, and T. Nakazawa, 1989: Dynamics of super cloud clusters, westerly wind bursts, 30–60 day oscillations and ENSO: A unified view. *J. Meteor. Soc. Japan*, **67**, 205–219.
- Lawrence, D. M., and P. J. Webster, 2002: The boreal summer intraseasonal oscillation: Relationship between northward and eastward movement of convection. *J. Atmos. Sci.*, **59**, 1593–1606.
- Liebmann, B., G. N. Kiladis, C. S. Vera, A. C. Saulo, and L. M. V. Carvalho, 2004: Subseasonal variations of rainfall in the vicinity of the South American low-level jet stream and comparison to those in the South Atlantic convergence zone. *J. Climate*, **17**, 3829–3842.
- Lin, J.-L., and Coauthors, 2006: Tropical intraseasonal variability in 14 IPCC AR4 climate models. Part I: Convective signals. *J. Climate*, **19**, 2665–2690.
- Liu, P., B. Wang, K. R. Sperber, T. Li, and G. A. Meehl, 2005: MJO in the NCAR CAM2 with the Tiedtke convective scheme. *J. Climate*, **18**, 3007–3020.
- , and Coauthors, 2009: Tropical intraseasonal variability in the MRI-20km60L AGCM. *J. Climate*, **22**, 2006–2022.
- Louis, J., 1979: A parametric model of vertical eddy fluxes in the atmosphere. *Bound.-Layer Meteor.*, **17**, 187–202.
- Madden, R. A., and P. R. Julian, 1971: Detection of a 40–50 day oscillation in the zonal wind in the tropical Pacific. *J. Atmos. Sci.*, **28**, 702–708.
- , and —, 1972: Description of global-scale circulation cells in the tropics with a 40–50 day period. *J. Atmos. Sci.*, **29**, 1109–1123.
- , and —, 1994: Observations of the 40–50 day tropical oscillation—A review. *Mon. Wea. Rev.*, **122**, 814–837.
- Maloney, E. D., and D. L. Hartmann, 1998: Frictional moisture convergence in a composite life cycle of the Madden–Julian oscillation. *J. Climate*, **11**, 2387–2403.
- , and —, 2001: The sensitivity of intraseasonal variability in the NCAR CCM3 to changes in convective parameterization. *J. Climate*, **14**, 2015–2034.
- , and A. H. Sobel, 2004: Surface fluxes and ocean coupling in the tropical intraseasonal oscillation. *J. Climate*, **17**, 4368–4386.
- Masunaga, H., M. Satoh, and H. Miura, 2008: A joint satellite and global cloud-resolving model analysis of a Madden-Julian Oscillation event: Model diagnosis. *J. Geophys. Res.*, **113**, D17210, doi:10.1029/2008JD009986.
- Mellor, G. L., and T. Yamada, 1974: A hierarchy of turbulence closure models for planetary boundary layers. *J. Atmos. Sci.*, **31**, 1791–1806.
- Miura, H., M. Satoh, T. Nasuno, A. T. Noda, and K. Oouchi, 2007: A Madden-Julian oscillation event realistically simulated by a global cloud-resolving model. *Science*, **318**, 1763–1765.
- Nakajima, T., M. Tsukamoto, Y. Tsushima, A. Numaguti, and T. Kimura, 2000: Modeling of the radiative process in an atmospheric general circulation model. *Appl. Opt.*, **39**, 4869–4878.
- Nakanishi, M., and H. Niino, 2006: An improved Mellor–Yamada level-3 model: Its numerical stability and application to a regional prediction of advection fog. *Bound.-Layer Meteor.*, **119**, 397–407.
- Nakazawa, T., 1988: Tropical super clusters within intraseasonal variations over the western Pacific. *J. Meteor. Soc. Japan*, **66**, 823–836.
- Nasuno, T., H. Miura, M. Satoh, A. T. Noda, and K. Oouchi, 2009: Multi-scale organization of convection in a global numerical simulation of the December 2006 MJO event using explicit moist processes. *J. Meteor. Soc. Japan*, **87**, 335–345.
- Neelin, J. D., I. M. Held, and K. H. Cook, 1987: Evaporation wind feedback and low-frequency variability in the tropical atmosphere. *J. Atmos. Sci.*, **44**, 2341–2348.
- Rui, H., and B. Wang, 1990: Development characteristics and dynamic structure of tropical intraseasonal convection anomalies. *J. Atmos. Sci.*, **47**, 357–379.
- Satoh, M., T. Matsuno, H. Tomita, H. Miura, T. Nasuno, and S. Iga, 2008: Nonhydrostatic icosahedral atmospheric model (NICAM) for global cloud resolving simulations. *J. Comput. Phys.*, **227**, 3486–3514.
- Slingo, J. M., and Coauthors, 1996: Intraseasonal oscillations in 15 atmospheric general circulation models: Results from an AMIP diagnostic subproject. *Climate Dyn.*, **12**, 325–357.
- Sperber, K. R., 2003: Propagation and the vertical structure of the Madden–Julian Oscillation. *Mon. Wea. Rev.*, **131**, 3018–3037.
- Tomita, H., and M. Satoh, 2004: A new dynamical framework of nonhydrostatic global model using the icosahedral grid. *Fluid Dyn. Res.*, **34**, 357–400.
- Waliser, D. E., C. Jones, J. K. Schemm, and N. E. Graham, 1999: A statistical extended-range tropical forecast model based on the slow evolution of the Madden–Julian Oscillation. *J. Climate*, **12**, 1918–1939.
- Wang, B., 1988: Dynamics of tropical low-frequency waves: An analysis of the moist Kelvin wave. *J. Atmos. Sci.*, **45**, 2051–2065.
- , and H. Rui, 1990: Synoptic climatology of transient tropical intraseasonal convective anomalies: 1975–1985. *Meteor. Atmos. Phys.*, **44**, 43–61.
- , and T. Li, 1994: Convective interaction with boundary-layer dynamics in the development of a tropical intraseasonal system. *J. Atmos. Sci.*, **51**, 1386–1400.
- Weickmann, K. M., 1983: Intraseasonal circulation and outgoing longwave radiation modes during Northern Hemisphere winter. *Mon. Wea. Rev.*, **111**, 1838–1858.
- Wheeler, M. C., and H. H. Hendon, 2004: An all-season real-time multivariate MJO index: Development of an index for monitoring and prediction. *Mon. Wea. Rev.*, **132**, 1917–1932.
- Yasunari, T., 1979: Cloudiness fluctuation associated with the Northern Hemisphere summer monsoon. *J. Meteor. Soc. Japan*, **57**, 227–242.
- Zhang, C., 2005: Madden-Julian oscillation. *Rev. Geophys.*, **43**, RG2003, doi:10.1029/2004RG000158.
- Ziemiański, M. Z., W. W. Grabowski, and M. W. Moncrieff, 2005: Explicit convection over the western Pacific warm pool in the Community Atmospheric Model. *J. Climate*, **18**, 1482–1502.